Nanoscale

PAPER

Check for updates

MgH₂ nanoparticles confined in reduced graphene oxide pillared with organosilica: a novel type of hydrogen storage material†

Feng Yan, [ID] [a] Estela Moretón Alfonsín,[a] Peter Ngene, [ID] [b] Sytze de Graaf,[a] Oreste De Luca,[a] Huatang Cao,[c] Konstantinos Spyrou, [ID] [d] Liqiang Lu,[c] Eleni Thomou, [ID] [a,d] Yutao Pei, [ID] [c] Bart J. Kooi,[a] Dimitrios P. Gournis, [ID] [d,e] Petra E. de Jongh [ID] [b] and Petra Rudolf [ID] *[a]

Hydrogen is a promising alternative fuel that can push forward the energy transition because of its high energy density (142 MJ kg⁻¹), variety of potential sources, low weight and low environmental impact, but its storage for automotive applications remains a formidable challenge. MgH₂, with its high gravimetric and volumetric density, presents a compelling platform for hydrogen storage; however, its utilization is hindered by the sluggish kinetics of hydrogen uptake/release and high temperature operation. Herein we show that a novel layered heterostructure of reduced graphene oxide and organosilica with high specific surface area and narrow pore size distribution can serve as a scaffold to host MgH₂ nanoparticles with a narrow diameter distribution around ~2.5 nm and superior hydrogen storage properties to bulk MgH₂. Desorption studies showed that hydrogen release starts at relatively low temperature, with a maximum at 348 °C and kinetics dependent on particle size. Reversibility tests demonstrated that the dehydrogenation kinetics and re-hydrogenation capacity of the system remains stable at 1.62 wt% over four cycles at 200 °C. Our results prove that MgH₂ confinement in a nanoporous scaffold is an efficient way to constrain the size of the hydride particles, avoid aggregation and improve kinetics for hydrogen release and recharging.

1. Introduction

Today, the major source of energy is fossil fuels, the burning of which leads to global warming and climate change.[1,2] Hydrogen has been proposed as an alternative fuel already for several decades, since it represents an ideal zero-carbon energy carrier with a higher delivered energy-per-mass ratio (120 kJ g⁻¹) than conventional fuels such as petroleum (43.6 kJ g⁻¹) or coal (39.3 kJ g⁻¹).[3] Also, no CO_2 or NO_x are produced in its combustion: the only byproduct is water vapor.[4] However, storage for automotive use remains a formidable scientific

challenge due to the demanding high gravimetric and volumetric capacity required to satisfy competitive refueling needs.[5–7] Magnesium hydride, MgH₂, represents a particularly compelling platform as a solid-state hydrogen storage material owing to its high theoretical storage capacity (7.6 wt% and 110 g L⁻¹) and outstanding reversibility which can potentially fulfill the requirements for fueling cars.[8,9] Moreover, magnesium is the eighth most abundant element in the Earth's mantle, and can therefore be considered a sustainable building block for a hydrogen storage material.[10]

Magnesium hydride still poses obstacles to the practical application, since its thermodynamic stability with an enthalpy of approximately −75 kJ mol⁻¹ leads to high operation temperatures.[11] In addition, the sluggish hydrogen absorption-desorption kinetics results in long times for the hydrogenation and dehydrogenation processes.[12] The inherently low thermal conductivity[13] (2–8 W (m K)⁻¹) also represents a difficulty for efficient use in this context. Nanostructuring of MgH₂ is a most effective strategy to lower the kinetic barrier,[14] since the large surface-to-volume ratio of the particles shortens the distances hydrogen atoms have to diffuse over.[15–17] Theoretical calculations and experimental studies have demonstrated that MgH₂ particle sizes of less

[a]Zernike Institute for Advanced Materials, University of Groningen, Nijenborgh 4, 9747 AG Groningen, the Netherlands. E-mail: p.rudolf@rug.nl
[b]Materials Chemistry and Catalysis, Debye Institute for Nanomaterials Science, Utrecht University, Universiteitsweg 99, 3584 CG Utrecht, the Netherlands
[c]Engineering and Technology Institute Groningen, University of Groningen, Nijenborgh 4, 9747AG Groningen, the Netherlands
[d]Department of Materials Science and Engineering, University of Ioannina, 45110 Ioannina, Greece
[e]School of Chemical and Environmental Engineering, Technical University of Crete, 73100 Chania, Crete, Greece
†Electronic supplementary information (ESI) available. See DOI: https://doi.org/10.1039/d4nr01524j

than 5 nm lead to a significant enhancement of hydrogen adsorption/desorption kinetics.[18–20] However, MgH_2 nanoparticles have the tendency to minimize their surface energy by agglomeration when the temperature is high enough and this deteriorates the kinetic properties, leading to the slower cycling.[21,22] Confinement of MgH_2 particles in nanoporous supports has been demonstrated to be an effective way to improve hydrogen desorption properties, since the particle size can be easily controlled by modifying the pore size of the scaffolds, and the direct inter-particle contact is avoided, which can further prevent particle agglomeration.[23–25] Furthermore, the application of lightweight materials of high thermal conductivity can additionally counterbalance the loss of capacity and enhance the sluggish hydrogen sorption kinetics.[26,27]

Graphene, a two-dimensional material with a thickness of one atomic layer, has attracted wide attention in hydrogen storage because of its unique 2D structure, light weight, and outstanding thermal conductivity (5300 W m^{-1} K^{-1}).[28–30] In addition, graphene also acts as a catalyst for hydrogen dissociation/recombination.[31] Given these advantages, graphene has been combined with magnesium hydride through different methods, such as ball milling,[31] wrapping,[32,33] assembling,[26] confinement,[9] etc. However, MgH_2 particles with a size less than 5 nm combined with graphene have not been achieved so far.

Inorganic–organic hybrids with organosilica building blocks prepared by surfactant directed sol–gel reaction of bridged organosilane precursors represent a new class of mesoporous materials.[34,35] In these hybrids, the organosilica functional groups can be integrated into the pore walls *via* the appropriate selection of organic precursors, and the pore size can be tuned *via* the selection of the surfactant.[36] Because of their high surface areas, controllable mesoscale porous structure, light-harvesting properties and the possibility to achieve a high thermal stability by selecting the appropriate bridge group, these mesoporous organosilicas are promising for hydrogen storage.[37,38] Kalantzopoulos *et al.*[39] investigated both theoretically and experimentally phenylene-bridged organosilica in this context, and demonstrated that the pore size distribution appears to be the predominant factor for hydrogen storage and that reversible hydrogen adsorption capacities up to 2.1 wt% can be realized at 6 MPa and 77 K.

Herein, we combine the advantages of graphene, or more precisely of reduced graphene oxide, rGO, and organosilica building blocks in a novel pillared heterostructure, which we synthesized by surfactant-directed sol–gel reaction of organosilica precursors in the interlayer space of graphene oxide, followed by removal of the soft template by pyrolysis. In this material, rGO assures thermal conductivity and a catalytic effect on MgH_2, while the organosilica pillars serve to confine the nanometer sized MgH_2 particles and prevent them from aggregating. As a result, MgH_2 crystals with an average particle size of ~2.5 nm were grown in this heterostructure and showed outstanding hydrogen desorption properties. In addition, *in situ* X-ray photoelectron spectroscopy was

employed to elucidate structural changes during the dehydrogenation process and to gain insight into the dehydrogenation mechanism.

2. Experimental section

2.1. Materials

Graphite flakes (<20 μm), potassium chlorate ($KClO_3$, ≥99.0%), dodecylamine (≥99.0%), 1,4-bis(triethoxysilyl)benzene (BTB, 99.0%), 1-butanol (anhydrous, 99.8%), tetrahydrofuran (anhydrous, 99.9%), and di-*n*-butylmagnesium ($MgBu_2$, 1.0 M in heptane) were acquired from Sigma-Aldrich. Sulfuric acid (H_2SO_4, 95.0–97.0%) and nitric acid (HNO_3, 65.0%) were purchased from Boom BV. Milli-Q water (resistivity 18 MΩ cm, 25 °C) was freshly produced before use. All the chemicals were used as received.

2.2 Synthesis of MgH_2/rGO-BTB nanocomposites

The layered heterostructure of reduced graphene oxide and organosilica, rGO-BTB, was prepared with a soft-template method[40] and the experimental details are described in the ESI.†
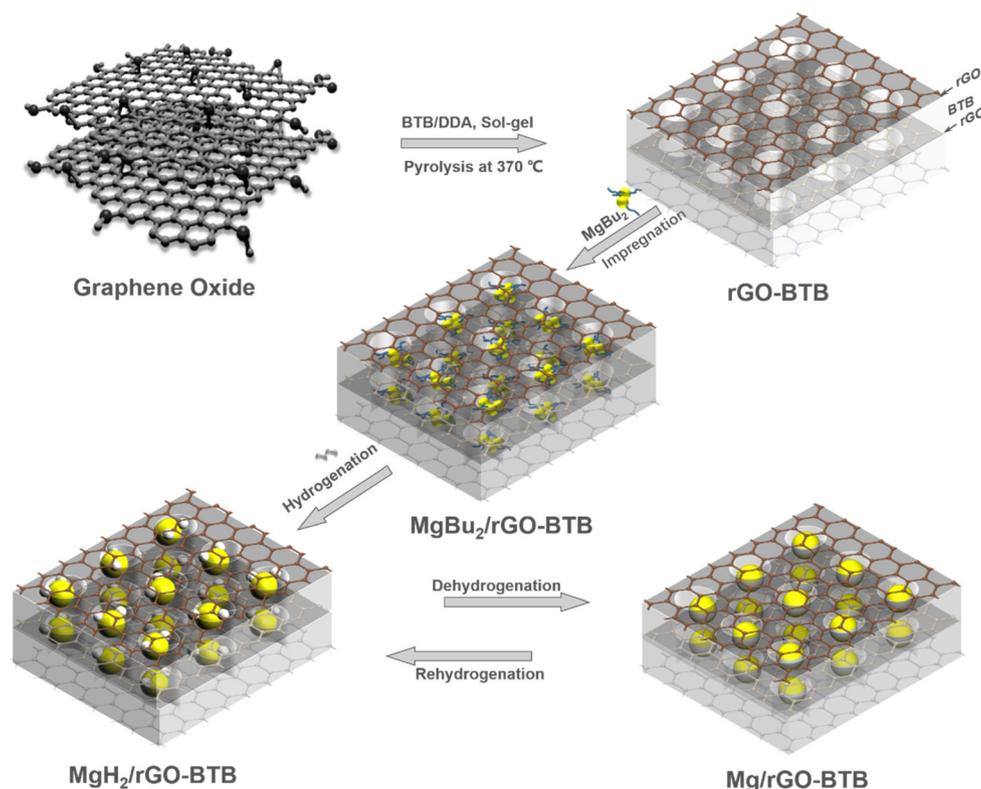
The MgH_2/rGO-BTB nanocomposites were prepared by the so-called bottom-up method[41] as indicated in Scheme 1. Sample handling and storage were conducted under an inert atmosphere in an argon-filled glovebox (Lab 2000, Etelua Intertgas System Co., Ltd) with a gas-circulation system. Before being brought in contact with $MgBu_2$, rGO-BTB was vacuum dried at 180 °C for 3 h to eliminate all moisture from the porous structure. rGO-BTB was impregnated with $MgBu_2$ with intermittent vacuum evaporation of the excess solvent (heptane) to absorb the maximum amount. $MgBu_2$/rGO-BTB was transferred from the airtight flask to a cylindrical quartz container and sealed in an autoclave. The precursors in the autoclave were hydrogenated at 55 bar H_2 pressure at 180 °C for 10 h following the reaction $MgBu_2 + H_2 \rightarrow MgH_2 + 2C_4H_{10}\uparrow$. Two batches were synthesized with 10 wt% and 20 wt% Mg loading of the nanocomposites, respectively, denoted as MgH_2/rGO-BTB-10 and MgH_2/rGO-BTB-20 in the following.

2.3 Thermal desorption and regeneration

The hydrogen desorption properties of MgH_2/rGO-BTB were studied by temperature programmed desorption (TPD) using a Micromeritics AutoChem II 2920 apparatus equipped with a TCD detector in conjunction with mass spectrometry. The MgH_2/rGO-BTB composites were loaded without air exposure, and the H_2 partial pressure and TCD signal were recorded while applying a constant temperature rate of 5 °C min^{-1} from 25 to 500 °C with 25 mL min^{-1} Ar flow.

Then we performed rehydrogenation/dehydrogenation experiments where the starting material was cycled at different temperatures to check for recyclability. Here we report in detail on the experiments where Mg/rGO-BTB was exposed in the autoclave to 12 bar H_2 pressure at 180 °C for 18 h to obtain

Graphene Oxide

BTB/DDA, Sol-gel

Pyrolysis at 370 °C

rGO-BTB

MgBu$_2$

Impregnation

MgBu$_2$/rGO-BTB

Hydrogenation

Dehydrogenation

Rehydrogenation

MgH$_2$/rGO-BTB

Mg/rGO-BTB

Scheme 1 Schematic illustration of the preparation of MgH$_2$/Mg nanoparticles inside the rGO-BTB matrix to obtain MgH$_2$/rGO-BTB or Mg/rGO-BTB.

MgH$_2$/rGO-BTB and then dehydrogenated in the TPD setup at 200 °C; four cycles were performed.

2.4 Materials characterization

Fourier-transform infrared spectroscopy (FTIR) spectra (resolution of 4 cm^{-1}, 32 scans) were acquired using a Bruker Vertex 70 spectrometer in the 500–4000 cm^{-1} range. X-ray diffraction (XRD) spectra were collected using a D8 Advance Bruker diffractometer with Cu K$_\alpha$ radiation (λ = 1.5418 Å) employing a 0.25° divergent slit and a 0.125° anti-scattering slit; the patterns were recorded in the 2θ range from 2° to 80°, with steps of 0.02° and a counting time of 2 s per step. With the air sensitive samples (MgH$_2$/rGO-BTB), a dome-shaped airtight sample holder was used to prevent the reaction with air during the measurement, and the loading of the sample in the holder was performed in an argon-filled glove box,[42] and the patterns were recorded in the 2θ range from 10° to 80°with a step of 0.017° and a time step of 60 s for a total of 30 min per scan. The nitrogen adsorption–desorption isotherms were measured at −196 °C on a Micromeritics ASAP 2420 V2.05 porosimeter. All samples were degassed overnight at 120 °C under vacuum before analysis. The specific surface area was evaluated with the Brunauer–Emmett–Teller (BET) model by fitting the N$_2$ adsorption isotherm; the pore volume was determined at P/P_0 = 0.995 and the pore size distribution was analyzed by the non-local density functional theory (NLDFT) method.[43]

Scanning electron microscopy (SEM) measurements were performed with a FEI Philips FEG-XL30s microscope.

A probe and image Cs aberration corrected 30–300 kV Thermo Fisher Scientific Thenis Z (scanning) transmission electron microscope (S/TEM) equipped with the dual X-ray detector was employed for the structural and MgH$_2$ particle size characterization. The acceleration voltage was set at 300 kV. Images were acquired using high-angle annular dark-field (HAADF)-STEM (21 mrad convergence semi-angle, 50 pA probe current, 31–186 mrad collection angles of the HAADF detector), bright-field TEM and dark-field TEM. Elemental maps were acquired using energy dispersive X-ray spectroscopy (EDS)-STEM. X-ray photoelectron spectroscopy (XPS) measurement of rGO-BTB was performed with a SSX-100 (Surface Science Instrument) spectrometer equipped with a monochromatic Al K$_\alpha$ X-ray source ($h\nu$ = 1486.6 eV). The measurement chamber pressure was maintained at 1×10^{-9} mbar during data acquisition; the photoelectron take-off angle was 37° with respect to the surface normal. The diameter of the analyzed area was 1000 μm; and the energy resolution was 1.26 eV. The rGO-BTB sample was prepared by being dispersed in chloroform and drop-casted on a thin gold film, grown on mica.[44] *In situ* XPS spectra of MgH$_2$/rGO-BTB-10 were collected by employing a monochromatic Al K$_\alpha$ X-ray source and a hemispherical electron analyzer (Scienta R4000). The spectra of wide scans and core level regions were acquired at a base

pressure of 9×10^{-10} mbar, and the overall energy resolution was 0.35 eV. MgH$_2$/rGO-BTB-10 sample was dispersed in anhydrous tetrahydrofuran and drop-casted on a thin gold film grown on mica[44] in an argon-filled glove box, and then transferred to the load-lock chamber under Ar atmosphere. Spectra were acquired after annealing at 200 and 300 °C for 2 hours. XPS spectral analysis included a Shirley background subtraction and fitting with a minimum number of peaks consistent with the expected composition of the probed volume, taking into account the experimental resolution. Peak profiles were taken as a convolution of Gaussian and Lorentzian functions; with the help of the least squares curve-fitting program WinSpec (LISE, University of Namur, Belgium). Binding energies (BEs) were referenced to Au 4f$_{7/2}$ photoemission peak centered at a binding energy of 84.0 eV and are accurate to ±0.1 eV when deduced from the fitting procedure.[45] All measurements were carried out on freshly prepared samples; three different spots were measured on each sample to check for reproducibility.

3. Results and discussion

3.1 Chemical and morphological characterizations of the rGO-BTB heterostructure matrixes

It is important to verify whether or not the composition, structure and morphology of rGO-BTB heterostructure agrees with those reported in previous studies.[40] To this end, at each stage of the synthesis, the materials were characterized by a variety of techniques, firstly by FTIR to confirm the successful incorporation of the dodecylamine and the silica precursor BTB in the interlayer space, as shown in Fig. S1(a).† Compared to the spectra of GO, the spectrum of dodecylamine-intercalated GO shows two additional peaks at 2847 cm^{-1} and 2919 cm^{-1} that are ascribed to the asymmetric and symmetric stretching vibrations of C–H bonds.[46] Another additional peak located at 1560 cm^{-1} is due to the N–H vibrations of the dodecylamine and verifies that dodecylamine is present in the layered structure. A confirmation of the presence of organosilica matrix in the composite comes from the bands centered at 520 cm^{-1}, 1065 cm^{-1} and 1151 cm^{-1}, which correspond to Si–O–Si vibrations, as well as from the peaks at 690 cm^{-1} and 950 cm^{-1}, due to the O–Si–O stretching modes.[47] After calcination, the broad peak centered at 3400 cm^{-1}, ascribed to the –OH stretching vibration and stretching vibration of C–H, vanishes.[48] This, together with the disappearance of the band centered at 1560 cm^{-1} attributed to N–H bonds, indicates that during the pyrolysis process dodecylamine and the functional groups on the surface of graphene oxide were removed.[40]

The successful intercalation of dodecylamine and BTB in the interlayer space of GO can be further confirmed by XRD, which allows to estimate the interlayer distance between the graphene oxide platelets, as shown in Fig. S1(b).† By applying the Bragg equation, one can derive the basal d_{001}-spacing, which in pristine graphene oxide amounts to 7.6 Å, but becomes 18.5 Å after intercalation with dodecylamine.[47] This

basal plane spacing corresponds to an interlayer separation Δ = 18.5–6.1 Å = 12.4 Å, where 6.1 Å represents the thickness of a single GO layer.[49] This value is in accordance with the chain length of dodecylamine. For GO intercalated with dodecylamine and BTB, the basal plane spacing is even larger, namely 27.0 Å, and the corresponding interlayer separation Δ = 27.0–6.1 Å = 20.9 Å. This points to successful further expansion of the interlayer space and suggests the formation of a silica network from BTB. For the heterostructure rGO-BTB, there is no sharp 001 diffraction at lower angles (2–10°), but a very broad peak can be observed. This indicates that the graphene layers are no longer stacked but exfoliated in thin platelets of very few layers due to the violent expansion upon heating rGO-BTB.

To verify the chemical integrity as well as the types of chemical bonds in rGO-BTB, X-ray photoelectron spectroscopy (XPS) was employed. The overview spectrum attests to the presence of all the expected elements (Fig. S2(a)†). The spectrum of the C 1s core level region of rGO-BTB, shown in Fig. S2(b),† shows four contributions: the spectral signature of the C=C bonds of graphene is centered at a BE of 284.8 eV, and makes up 70.4% of the total C 1s intensity. The contribution due to C–OH bonds, at a BE of 285.9 eV, represents 21.2% of the total C 1s intensity, while the contributions at BEs of 287.2 eV and 289.1 eV are respectively ascribed to the C=O and C(O)O bonds. The presence of Si–O–C bonds of BTB grafted to the oxygen-containing groups of the graphene oxide surface or to Si–O–Si bonds resulting from a sol–gel reaction between BTB molecules is supported by the Si 2p and Si 2s core level peaks in Fig. S2(c) and (d).† Taken together, the XPS spectra confirm that the reduced graphene oxide layers were successfully pillared with the silica precursor BTB by the sol–gel reaction.

The morphology of the obtained rGO-BTB composite was initially determined via scanning electron microscopy (SEM). As shown in Fig. 1(a), well-assembled multilayer platelets with smooth surfaces can be observed, and the sample consists of many such thin flakes owing to the partial exfoliation during the calcination process. The enlarged sectional view (Fig. 1(b)) further confirms that mesoporous organosilica must be dispersed in between layers leading to a very regular pillared structure.

Nitrogen adsorption–desorption measurements were performed to determine the surface area and to provide information on the pore structure. A typical isotherm is presented in Fig. 1(c). The sudden release of N$_2$ at $P/P_0 \approx 0.5$ gives rise to a type H4 hysteresis loop, commonly ascribed to slit-shaped pores in layered materials based on the IUPAC classification.[50] The adsorption branch of the isotherm reveals a type II plateau, and at low relative pressures, N$_2$ adsorption increases significantly with pressure, indicating that a significant amount of micropores/mesopores are accessible. The specific surface area (SSA) and pore volume were calculated to be 302 ± 4 m^2 g^{-1} and 0.14 cm^3 g^{-1}, respectively.

In order to further examine the structural characteristics, high-angle annular dark-field scanning transmission electron microscopy (HAADF-STEM) images of the rGO-BTB sample
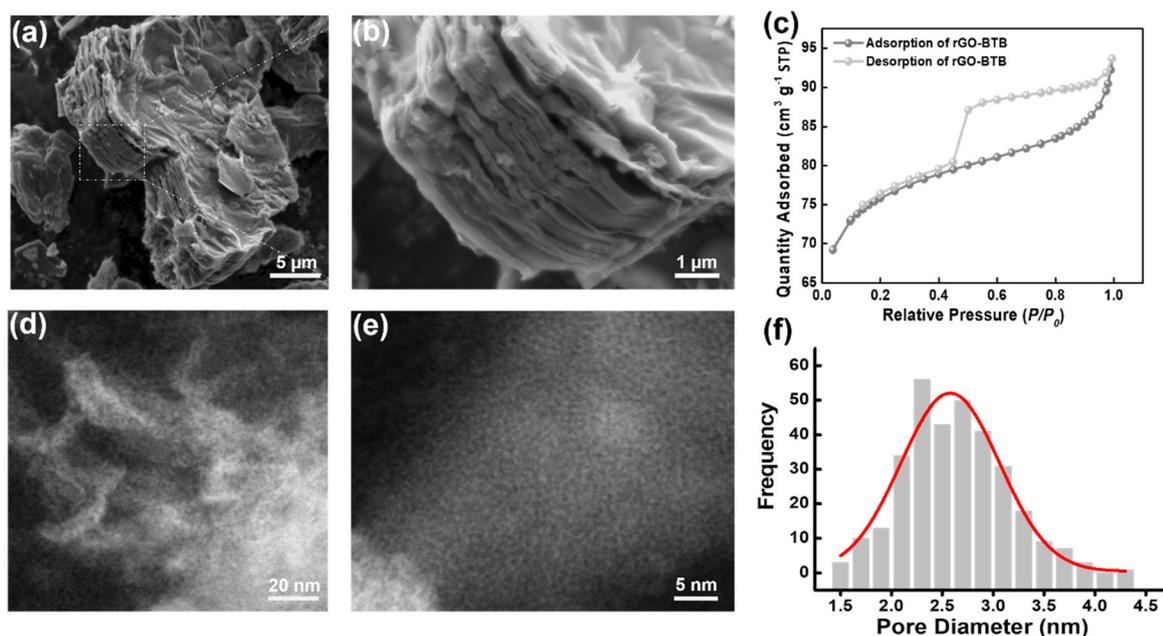
Fig. 1 (a) and (b) SEM images of rGO-BTB; (c) N$_2$ adsorption–desorption isotherm of rGO-BTB, inset BJH pore size distribution of rGO-BTB. (d) STEM image of rGO-BTB. (e) STEM image zoomed in from (d). (f) The pore size distribution calculated from (e).

were collected at low and high magnification and typical examples are shown in Fig. 1(d) and (e). In the lower magnification image (Fig. 1(d)), the mesopores are distributed homogeneously in the material, while in the higher magnification image (Fig. 1(e)) the nanoporous structure can be more clearly observed. The pore width distribution, determined by calculating the size of all pores visible in this image with the help of the Image J software, is shown in Fig. 1(f) and peaks at a pore size of 2.5 nm.

3.2 Evaluation of the magnesium hydride filled mesoporous heterostructure matrixes

Once sure that the desired porous structure was achieved, we proceeded with the growth of MgH$_2$ nanoparticles in the rGO-BTB mesoporous matrix, as shown in the schematic representation in Scheme 1, by first impregnating the latter with MgBu$_2$ and then hydrogenating (as described above in the Experimental section) for 10 h. Two batches, denoted with MgH$_2$/rGO-BTB-10 and MgH$_2$/rGO-BTB-20, were prepared, the first with 10 wt% of MgH$_2$ introduced into the rGO-BTB heterostructure and the second one with 20 wt%.

The X-ray diffraction patterns of pristine rGO-BTB and of rGO-BTB with the two different magnesium hydride loadings are shown in Fig. 2(a). For the pattern of MgH$_2$/rGO-BTB-20, the most intense diffraction peaks originate from the MgH$_2$ tetragonal phase.[25] The Scherrer equation[51] gives a particle size of 27 nm for MgH$_2$. Since the rGO-BTB matrix has a narrow pore size distribution around 2.5 nm, such big particles are likely grown on the outside surface of rGO-BTB flakes, unless the layers have locally ruptured forming a small cavity.[23] No diffraction peaks from MgH$_2$ can be noticed for

MgH$_2$/rGO-BTB-10, suggesting that no large particles grow outside the matrix in this case and that the MgH$_2$ nanoparticles, which were formed, have coherence lengths that are too small to diffract the X-rays.[25]

In order to gain further insight into the porous structure after the formation of MgH$_2$, nitrogen adsorption–desorption measurements were performed and the corresponding isotherms are shown in Fig. 2(b). The specific surface area and pore volumes were calculated and are listed in Table S1.† The BET specific surface areas and pore volumes are found to be smaller than for pristine rGO-BTB and decrease significantly with increasing amounts of MgH$_2$. This is mainly due to the blocking of the pores in the heterostructure by MgH$_2$ particles, which can be further confirmed by the NLDFT pore sized distribution evolutions in Fig. 2(c).[25] For MgH$_2$/rGO-BTB-10, the change of the isotherm was limited, testifying to a decrease of 38.0% of the specific surface area and 33.8% of the pore volume with respect to pristine rGO-BTB, which means the magnesium hydride nanoparticles do not fill all the pores. However, for MgH$_2$/rGO-BTB-20, the micropore volume decreased significantly (86.8% as compared to pristine rGO-BTB), while the mesoporous volume increased, indicating that the MgH$_2$ particles preferentially filled the micropores rather than the mesopores. The excess larger crystals on the outside surface of the rGO-BTB heterostructure lead to an increase of the mesoporous volume in agreement with the XRD result.

These conclusions are further supported by the field-emission scanning electron microscopy (FE-SEM) and transmission electron microscopy (TEM) images shown in Fig. 2(d–f) (MgH$_2$/rGO-BTB-10) and Fig. S3† (MgH$_2$/rGO-BTB-20) of the
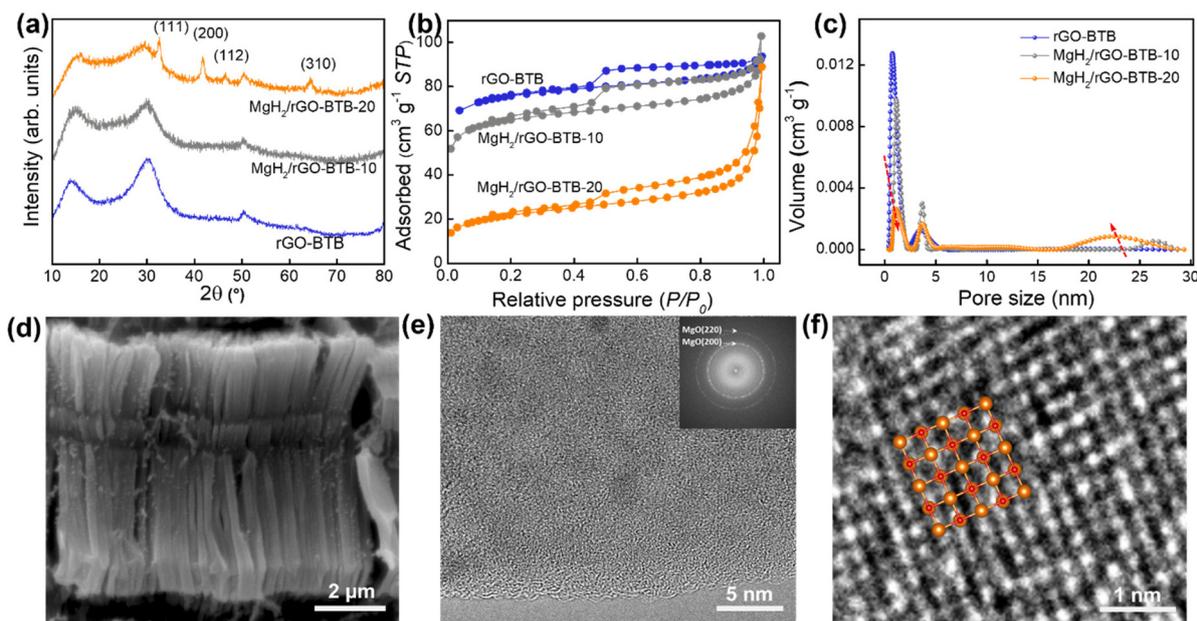
Fig. 2 (a) X-ray diffraction patterns, (b) N_2 adsorption–desorption isotherms and (c) NLDFT pore size distribution of rGO-BTB, MgH$_2$/rGO-BTB-10 and MgH$_2$/rGO-BTB-20. (d) SEM image of MgH$_2$/rGO-BTB-10; (e) TEM image of MgH$_2$/rGO-BTB-10, the insert shows the corresponding fast Fourier transform pattern; (f) HRTEM image of MgH$_2$/rGO-BTB-10, overlay: MgO atomic structure.

ESI.† The SEM image (Fig. 2(d)) shows that rGO-BTB in MgH$_2$/rGO-BTB-10 largely retains its original layered morphology, while hardly any agglomerated particles located on the outside of the layered structure can be observed. The bright-field TEM images (Fig. 2(e) and 3(a)) of MgH$_2$/rGO-BTB-10 show homogenously distributed particles throughout the rGO-BTB matrix, which have an MgO crystal structure as directly observable from the atomically resolved structure of a single particle (Fig. 2(f)) and the fast Fourier transform (FFT) of the entire collection of particles (inset of Fig. 2(e)) revealing the (111), (200) and (220) fcc MgO planes.[52] In contrast, the larger particles have not been oxidized, but in fact remained fully hydrogenated MgH$_2$ crystals, as the characteristic d(110) interlayer space of 0.321 nm of MgH$_2$ is visible in atomically resolved images, shown in Fig. S3(a) and (b).†[53] This evidence indicates that the sample transfer in air for the TEM measurements is most likely cause for the complete oxidation of small MgH$_2$ particles.[26]

Since the particle size is a significant parameter for the hydrogen storage properties of MgH$_2$ in the porous structure, the particle size distribution was extracted from the bright-field and dark-field TEM images of MgH$_2$/rGO-BTB-10 and MgH$_2$/rGO-BTB-20. In the bright-field TEM image (Fig. 3(a)) of MgH$_2$/rGO-BTB-10, the particle size distribution is centered at 2.5 nm, and in the dark-field TEM of the same batch, the particle size distribution peaked at 3.0 nm. As expected from the XRD results, the TEM images of MgH$_2$/rGO-BTB-20 (Fig. 3(d–f)) and MgH$_2$/rGO-BTB-20 (Fig. 3(d–f) and Fig. S3(b)†) show the several larger particles on the external surface of rGO-BTB. However, if one excludes these large particles from the calculation, the particle size distributions, shown in the insets of

Fig. 3(d) and (f), were again centered on 2.5 nm, as for MgH$_2$/rGO-BTB-10. The SEM images of MgH$_2$/rGO-BTB-20 (Fig. S3(c)†) seem to point to crystal growth from the inside of the porous structure to the external surface; a large amount of MgH$_2$ crystals can be distinguished on the surface and dendrites are seen to have grown from the inside outwards. HAADF-STEM images and EDS elemental maps, as presented in the bottom panel of Fig. 3, further verify the successful confinement of MgH$_2$ particles in the rGO-BTB heterostructure. Mg and C are homogeneously distributed in the material, while Mg is also dispersed in the porous structure and surrounded by C, in good agreement with the results of the other characterization techniques.

3.3 Hydrogen desorption properties of MgH$_2$/rGO-BTB composites

In order to explore hydrogen storage properties of MgH$_2$ particles confined in the rGO-BTB heterostructure, temperature programmed desorption (TPD) experiments of the bulk MgH$_2$ and of the two batches with different MgH$_2$ loading were carried out; the results are shown in Fig. 4(a). One observes that a temperature as high as 431 °C is needed for bulk MgH$_2$ to release H$_2$; such a high dehydrogenation temperature and sluggish kinetics are far from meeting the requirements for automotive applications. In contrast, MgH$_2$ particles confined in the mesoporous heterostructure show superior dehydrogenation properties: MgH$_2$/rGO-BTB-20 exhibits an onset temperature of desorption around 160 °C, 271 °C lower than the temperature threshold of bulk MgH$_2$. However, for the MgH$_2$/rGO-BTB-10, an onset temperature of 50 °C can be observed (Fig. 4(b)), an impressive 381 °C lower value than
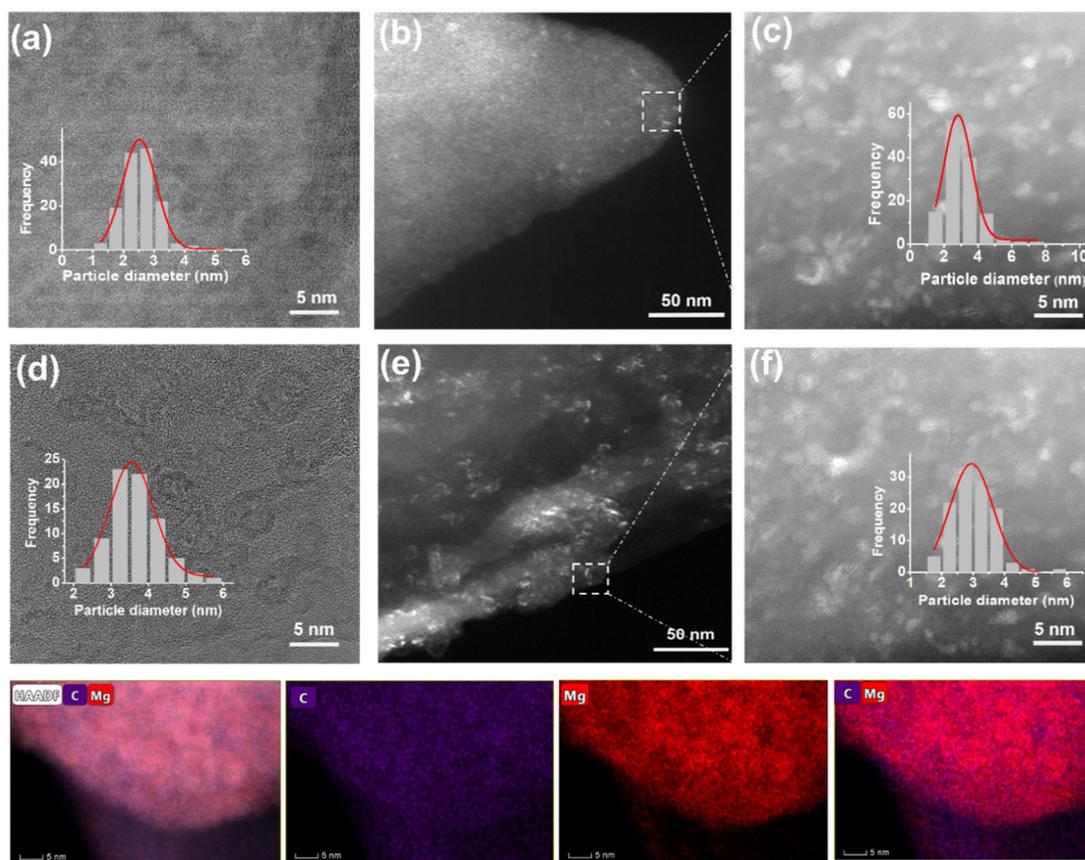
Fig. 3 (a) bright-field and (b) and (c) dark-field TEM images of MgH$_2$/rGO-BTB-10, the insets of (a) and (c) show the corresponding particle size distribution of the image. (d) bright-field and (e) and (f) dark-field TEM images of MgH$_2$/rGO-BTB-20, the insets of (d) and (f) show the corresponding particle size distribution of the image. The bottom panels: HAADF-STEM and EDS elemental maps for C, Mg, and C combined with Mg in MgH$_2$/rGO-BTB-10.

that of bulk MgH$_2$. This low onset is also evident in the detailed TDS spectrum collected in the temperature region of 40–100 °C and shown in Fig. S4.† Fig. 4(b) shows a plateau between 50–135 °C, while exhibiting an exponential growth after 135 °C, which is close to the onset temperature of MgH$_2$/rGO-BTB-20. That implies that the onset temperature for hydrogen release at 50 °C could be physisorbed H$_2$ in the unfilled mesopores, while 135 °C could be the temperature for the nanosized MgH$_2$ particles to start releasing hydrogen. The reason why the desorption of physisorbed H$_2$ is not visible for MgH$_2$/rGO-BTB-20, is clear from the BET results, which indicate that the mesoporous structure is largely blocked by the MgH$_2$ particles.

The superior dehydrogenation properties of MgH$_2$/rGO-BTB can be ascribed to the nanometer sized MgH$_2$ particles in the mesoporous heterostructure. Nanometer sized MgH$_2$ is thermodynamically less stable, resulting in lower activation energies for desorption, and therefore, a lower onset temperature than bulk MgH$_2$. In addition, nanometer sized MgH$_2$ crystals boost the kinetics of dehydrogenation because of the intrinsically short diffusion paths for hydrogen, which represent the rate-limiting step for the hydrogenation or dehydro-

genation processes. The catalytic properties of the porous scaffold might also play a role in the improvement of the kinetics.[54] The unsaturated carbon atoms from reduced graphene oxide bind with MgH$_2$ located between the layers, resulting in electron transfer from Mg to rGO and thus weaker Mg–H bonds, a scenario in which hydrogen may be released with smaller activation energy.[55] Furthermore, while the TPD desorption isotherm peak of MgH$_2$/rGO-BTB-10 is symmetric, the peak of MgH$_2$/rGO-BTB-20 is broader and asymmetric, pointing to two populations of nanoparticles with different desorption kinetics. The small shoulder at higher temperature close to the desorption temperature of bulk MgH$_2$ is attributed to the larger particles outside the rGO-BTB matrix. This TPD profile is hence consistent with the bimodal particle size distribution shown by the TEM study (Fig. 3(d)). The desorption is not completed at 470 °C: desorption from MgH$_2$ located outside of the matrix and the ordered mesoporous heterostructure continues at higher temperature.[56] However, the temperature for maximum hydrogen desorption of 348 °C for the batch of MgH$_2$-rGO-BTB-10 is higher than what previous work[16] found for particle sizes <10 nm. This indicates that not only the particle size influences the maximum desorption
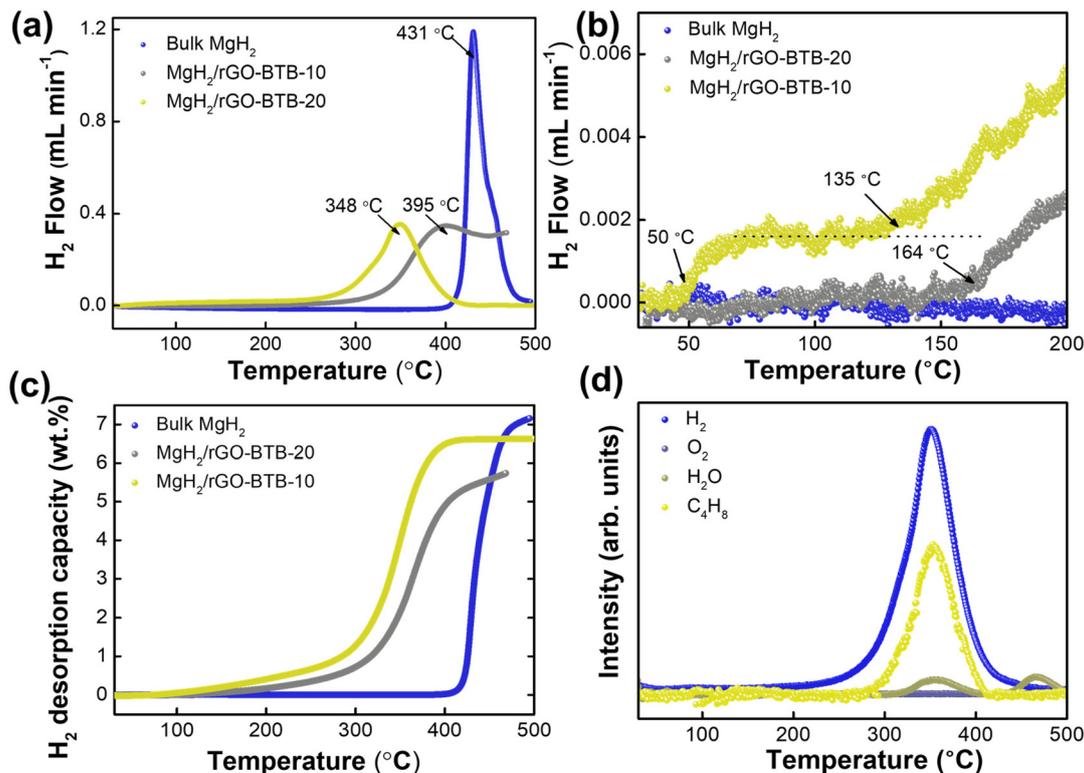
Fig. 4 (a) Temperature programmed desorption (TPD) spectra of bulk MgH$_2$ and MgH$_2$ particles confined in the rGO-BTB structure, recorded with a heating rate of 5 °C min^{-1}. (b) TPD spectra of bulk MgH$_2$ and confined MgH$_2$ particles in rGO-BTB structures from 30 °C to 200 °C, enlarged view of the onset of desorption in (a). (c) Hydrogen desorption capacity of bulk MgH$_2$ and MgH$_2$ particles embedded in the rGO-BTB structure from 30 °C to 500 °C; the capacity is based on the confined MgH$_2$ weight. (d) Mass spectrometry analysis upon heating to 500 °C for MgH$_2$/rGO-BTB-10.

temperature, but also the interaction between the MgH$_2$ particles and the rGO matrix as well as the pillaring structures may affect hydrogen desorption properties of MgH$_2$. In future work different pillars will have to be examined to clarify this issue.

The dehydrogenation capacities of confined MgH$_2$ and the bulk MgH$_2$ are presented in Fig. 4(c). It should be noted that the desorption capacity of the MgH$_2$/rGO-BTB was obtained by excluding the weight percentage of the heterostructure matrixes to compare the hydrogenation properties of the confined Mg nanoparticles. The desorption capacity of bulk MgH$_2$ reaches 7.1 wt%; in contrast, the confined MgH$_2$ in the heterostructure shows relatively lower desorption capacity. MgH$_2$/rGO-BTB-10 has around 6.6 wt% of reversible H$_2$ storage capacity related to confined MgH$_2$, while for MgH$_2$/rGO-BTB-20, the desorption capacity reaches only 5.7 wt%, presumably because the larger MgH$_2$ crystals located outside of the matrix become partially oxidized or reacted with residual oxygen-containing groups on the external surface of the matrix.[57]

We collected TPD-MS spectra to monitor the chemical species released during the MgH$_2$/rGO-BTB-10 dehydrogenation process; the results are shown in Fig. 4(d). As expected, the hydrogen signal is the largest one; the release of butane was expected because it is the byproduct of the hydride elimin-

ation reaction that transforms the MgBu$_2$ solution into magnesium hydride.[24] There is no oxygen signal detected, which means no O$_2$ is released from the heterostructure and no O$_2$ contamination is evident. However, desorption peaks related to water were observed in similar positions to those of hydrogen, namely centered at 350 °C and 475 °C; this might point to a water-producing reaction involving the decomposition Mg(OH)$_2$ or the reaction between the dehydrogenated Mg and oxygen-containing groups on the porous matrix.

3.4 Hydrogen storage reversibility of MgH$_2$/rGO-BTB-10 composite

The reversibility of the performance of hydrogen storage materials is considered as an important requisite for automotive application.[58] Mesoporous silica has been proposed as a promising nanoscale template for metal hydrides, such as NaBH$_4$,[59] NaAlH$_4$,[60] and LiBH$_4$[61] by melt infiltration, however the reaction between the silanol groups in the pore channel and metal hydrides at high temperature resulted in an irreversibility loss of hydrogen storage capacity.[62] For the MgH$_2$/Mg hydrogen storage system, Zhu et al.[63] reported that MgH$_2$ confined in mesoporous silica shows excellent reversibility at 250 °C. In order to investigate the reversibility of MgH$_2$/rGO-BTB-10, the isothermal hydrogen absorption/desorption cycling measurements were car ried out at 200 °C, as
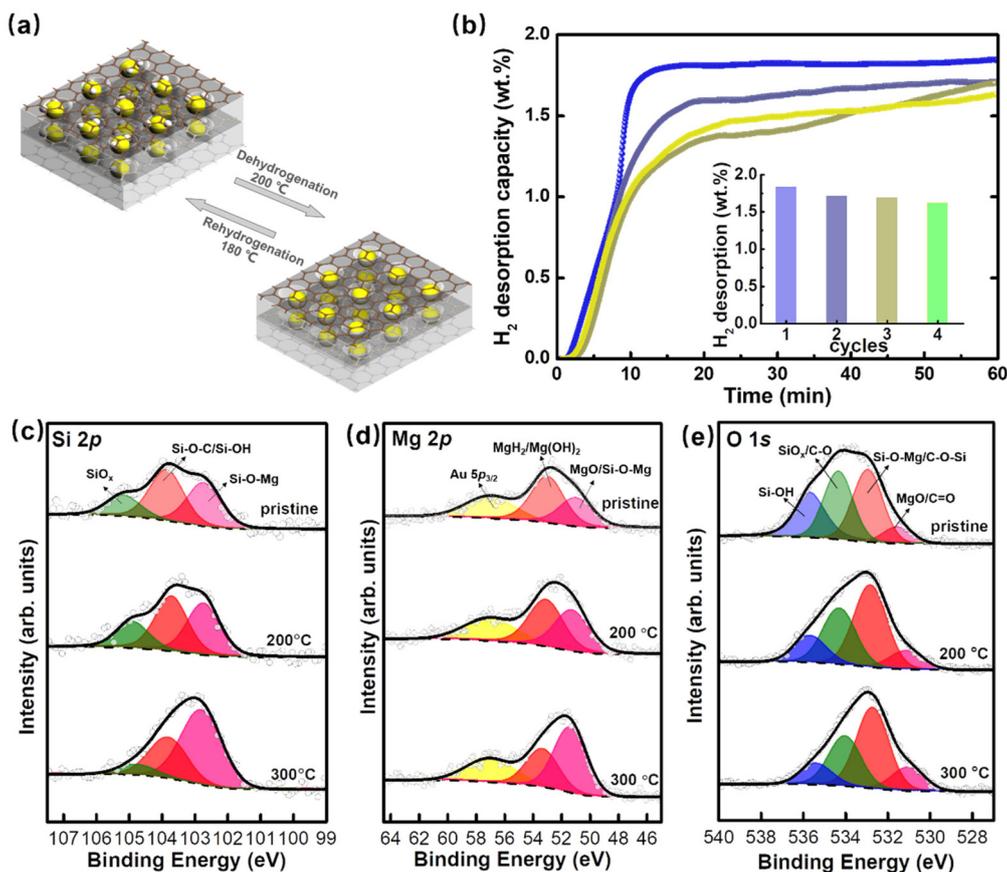
Fig. 5 (a) Schematic illustration of the rehydrogenation and dehydrogenation process of Mg/rGO-BTB-10 and MgH$_2$/rGO-BTB-10 composites. (b) Hydrogen desorption of reversibility measurement for MgH$_2$/rGO-BTB-10 at 200 °C (absorption at 180 °C; desorption at 200 °C), inset: the hydrogen desorption capacity value of each cycle. *In situ* X-ray photoelectron spectroscopy of the (c) Si 2p, (d) Mg 2p and (e) O 1s core level regions of MgH$_2$/rGO-BTB-10 after heating to different temperatures as indicated.

illustrated in Fig. 5(a). MgH$_2$/rGO-BTB-10 at 200 °C has a hydrogen storage capacity of 1.83 wt% during the first cycle and in the following three cycles, a high reversible capacity of 1.62 wt% was achieved, in other words, 88.5% of the original capacity was preserved (Fig. 5(b)). It is worth noting that the hydrogen was released within 20 min, indicating that the desorption kinetics did not degrade in these four cycles, indirectly confirming that the confinement of the nanoparticles in the heterostructure inhibits aggregation.[64] However, when dehydrogenation is performed at temperatures higher than 250 °C, MgH$_2$/rGO-BTB-10 is no longer stable and reversible hydrogen absorption/desorption is no more possible.

In order to gain insight into the chemical changes of MgH$_2$/rGO-BTB-10 with increasing temperature, we employed *in situ* X-ray photoelectron spectroscopy. The spectra of the Si 2p core level region are presented in Fig. 5(c); for pristine MgH$_2$/rGO-BTB-10 three contributions are needed in the fit: the spectral signature of Si–O–C overlaps with Si–OH centered at the BE of 103.6 eV, while the SiO$_x$ component can be observed centered at 105.2 eV.[65] The presence of Si–O–Mg bonds is confirmed by the component peaked at a BE of 102.6

eV.[66] After heating at 200 °C and consequent dehydrogenation, slight changes in the relative intensities of the three components in Si 2p core level spectrum can be observed; instead after dehydrogenation at 300 °C, the relative intensities of the components vary more dramatically: the intensity of the signal due to Si–O–Mg increases, while that of the components originating from C–O–Si/Si–OH and SiO$_x$ decreases, implying that the reaction between dehydrogenated Mg and the silanol groups could be responsible for the irreversibility of hydrogen storage.

The spectrum of the Mg 2p core level region of MgH$_2$/rGO-BTB-10 is shown in Fig. 5(d). It partially overlaps with the Au 5p$_{3/2}$ line of the substrate, peaked at 57.0 eV,[45] and can be fitted with two contributions centered at BEs of 50.9 eV and 52.8 eV, respectively. The latter contains the signals of MgH$_2$ and Mg(OH)$_2$, while the former is ascribed to Si–O–Mg/MgO.[67]

The O 1s core level region of MgH$_2$/rGO-BTB-10 is presented in Fig. 5(e), and contains four contributions: a first peak at a BE of 531.5 eV that derives from MgO/C=O;[68] a second one at a BE of 532.9 eV, which corresponds to the relatively electron-poor oxygen from Mg–O–Si/C–O–Si bonds, and two

contributions centered at 534.2 eV and 535.6 eV, stemming from SiO_x/C–O and Si-OH, respectively.[69]

After heating to 200 °C a slight decrease of the intensity of MgH_2/$Mg(OH)_2$ component of the Mg 2p core level can be observed, while that of the $Mg(OH)_2$ component remains stable at this temperature,[70] indicating the successful dehydrogenation of MgH_2. The concomitant small intensity increase of the MgO/Si–O–Mg component could explain why the hydrogen storage capacity is slightly lower in the consecutive cycles. However, after dehydrogenation at 300 °C, the narrower full width at half maximum (fwhm) of the Mg 2p and O 1s core level line signals more important chemical changes. A significant decrease of the spectral intensity due to MgH_2/$Mg(OH)_2$, and an important increase of that corresponding to MgO/Mg–O–Si can be observed in Mg 2p core level region, and indicate that the dehydrogenation of MgH_2 is accompanied by the decomposition of $Mg(OH)_2$ to give rise to Si–O–Mg bonds or MgO. In addition, the significant increase of the fingerprint of Si–O–Mg bonds in both Si 2p and O 1s core level photoemission signals, while the MgO/C=O intensity in O 1s core level hardly changes, imply that dehydrogenated Mg tends to react with Si–OH to form Si–O–Mg bonds instead of MgO.

Further spectral evidence confirms this picture: the photoemission spectra of the C 1s core level region of MgH_2/rGO-BTB-10 are shown in Fig. S5.† Since rGO-BTB is produced by calcination at 370 °C for 2 h, most of the C=O/O–C=O groups were removed in that synthesis step and the relatively thermostable bonds C–O/C–O–Si bonds remain in the framework; it is therefore no surprise that the intensity of the C=O/O–C=O component hardly decreases after heat treatments at 200 and 300 °C (Table S2†).[71] The presence of oxidized magnesium is instead further corroborated by the shape of the Mg KLL Auger peak, shown in Fig. S6:† already in the pristine sample there is not only the contributions at 310.2 eV deriving from $Mg(OH)_2$ and MgH_2 but also the spectral signature of MgO at 308.0 eV. The Mg KLL Auger line therefore points to a partial oxidation of the confined MgH_2 particles after hydrogenation and sample transport, despite all the precautions taken (described in the section on experimental details).[68] More importantly, the MgO component becomes dominant after heating to 300 °C, while the $Mg(OH)_2$ and MgH_2 strongly decrease. Both the Mg 2p photoemission spectrum and the Mg KLL Auger line give evidence for an increasing oxidation of magnesium when heated to 300 °C, corroborating the conclusion that the reaction between dehydrogenated Mg and the silanol groups degrades the recyclability at this high temperature. Based on the minor chemical changes at 200 °C, the reversible hydrogen storage of MgH_2/rGO-BTB-10 when not surpassing that temperature in the dehydrogenation could indicate that temperatures of 250 °C or higher are needed to activate the reaction between Si–OH and Mg. These findings suggest that calcination at higher temperature to remove the silanol groups and any residual oxygen-containing groups, or inactivation of the silanol groups by methylation[72] before magnesium hydride loading could be ways to realize reversible hydrogen storage at higher temperature in this type of hybrid.

4. Conclusions

A novel layered heterostructure of reduced graphene oxide and organosilica with high specific surface area and narrow pore size distribution was successfully synthesized by surfactant-directed sol–gel reaction of an organosilicon precursor in the interlayer space of graphene oxide. Porosimetry measurement and HAADF-STEM images revealed the mesoporous structures were with narrow pore size distribution of 2.5 nm, enabling the confinement of nanosized MgH_2 nanoparticles via wet impregnation with $MgBu_2$ followed by thermal hydrogenation. Due to the well-defined porous structure in the matrix, MgH_2 crystals were homogeneously distributed with the particle size of ∼2.5 nm. The onset of the hydrogen desorption is observed at low temperatures (135 °C), and exhibits maximum desorption at 348 °C. In addition, the cycling experiments show that efficient reversible 1.62 wt% hydrogen storage can be realized at 200 °C, indicating that the scaffold can efficiently inhibit nanoparticle aggregation and coalescence. At higher temperature, however, the hydrogen storage capacity is lost due to the gradual irreversible reaction of the Mg with the residual silanol groups. This MgH_2 nanoparticle confinement approach has promising prospects, and is compatible with the incorporation of catalytic or reactive additives in the porous matrix to further tune the thermodynamic and kinetic performance of the MgH_2 nanoparticles for hydrogen storage purposes.

Author contributions

P. Rudolf, P. de Jongh and D. Gournis conceived the study and finalized the manuscript. F. Yan conducted the experiments, the data analysis, and wrote the draft of the manuscript. P. Ngene performed the hydrogen storage experiments and their interpretation. E. M. Alfonsín, K. Spyrou and E. Thomou contributed to the material synthesis and characterization. S. de Graaf and B. J. Kooi performed the S/TEM characterization. O. De Luca collaborated in the XPS measurements. H. T. Cao, L. Q. Lu and Y. T. Pei participated in the SEM experiments. All authors discussed the results and commented on the manuscript.

Conflicts of interest

The authors declare no conflict of interest.

Acknowledgements

References

1 J. A. Turner, *Science*, 2004, **305**, 972.

2 D. A. J. Rand and R. M. Dell, *Hydrogen energy: challenges and prospects*, Royal Society of Chemistry, London, U.K., 2007.

3 T. G. Spiro, K. L. Purvis-Roberts and W. M. Stigliani, *Chemistry of the Environment*, University Science Books, Sausalito, CA, U.S.A., 2012.

4 C. J. Winter, *Int. J. Hydrogen Energy*, 2009, **34**, 1.

5 J. Tollefson, *Nature*, 2010, **464**, 1262.

6 M. A. DeLuchi, *Int. J. Hydrogen Energy*, 1989, **14**, 81.

7 A. Züttel, *Mater. Today*, 2003, **6**, 24.

8 D. Ross, *Vacuum*, 2006, **80**, 1084.

9 J. Zhang, S. Yan and H. Qu, *Int. J. Hydrogen Energy*, 2018, **43**, 1545.

10 M. E. Maguire and J. A. Cowan, *BioMetals*, 2002, **15**, 203.

11 K. Bohmhammel, U. Wolf, G. Wolf and E. Königsberger, *Thermochim. Acta*, 1999, **337**, 195.

12 J. Huot, G. Liang, S. Boily, A. Van Neste and R. Schulz, *J. Alloys Compd.*, 1999, **293**, 495.

13 J. Kapischke and J. Hapke, *Exp. Therm. Fluid Sci.*, 1998, **17**, 347.

14 P. E. de Jongh and P. Adelhelm, *ChemSusChem*, 2010, **3**, 1332.

15 R. W. Wagemans, J. H. van Lenthe, P. E. de Jongh, A. J. Van Dillen and K. P. de Jong, *J. Am. Chem. Soc.*, 2005, **127**, 16675.

16 Y. S. Au, M. K. Obbink, S. Srinivasan, P. C. Magusin, K. P. de Jong and P. E. de Jongh, *Adv. Funct. Mater.*, 2014, **24**, 3604.

17 V. Berube, G. Radtke, M. Dresselhaus and G. Chen, *Int. J. Energy Res.*, 2007, **31**, 637.

18 M. Paskevicius, D. A. Sheppard and C. E. Buckley, *J. Am. Chem. Soc.*, 2010, **132**, 5077.

19 Z. Zhao-Karger, J. Hu, A. Roth, D. Wang, C. Kübel, W. Lohstroh and M. Fichtner, *Chem. Commun.*, 2010, **46**, 8353.

20 P. Vajeeston, S. Sartori, P. Ravindran, K. Knudsen, B. Hauback and H. Fjellvag, *J. Phys. Chem. C*, 2012, **116**, 21139.

21 C. Zlotea, C. Chevalier-César, E. Léonel, E. Leroy, F. Cuevas, P. Dibandjo, C. Vix-Guterl, T. Martens and M. Latroche, *Faraday Discuss.*, 2011, **151**, 117.

22 P. E. De Jongh, Keeping out the oxygen, *Nat. Mater.*, 2011, **10**, 265.

23 K. J. Jeon, H. R. Moon, A. M. Ruminski, B. Jiang, C. Kisielowski, R. Bardhan and J. J. Urban, *Nat. Mater.*, 2011, **10**, 286.

24 T. K. Nielsen, K. Manickam, M. Hirscher, F. Besenbacher and T. R. Jensen, *ACS Nano*, 2009, **3**, 3521.

25 C. Zlotea, Y. Oumellal, S. J. Hwang, C. M. Ghimbeu, P. E. de Jongh and M. Latroche, *J. Phys. Chem. C*, 2015, **119**, 18091.

26 G. Xia, Y. Tan, X. Chen, D. Sun, Z. Guo, H. Liu, L. Ouyang, M. Zhu and X. Yu, *Adv. Mater.*, 2015, **27**, 5981.

27 G. Prieto, J. Zečević, H. Friedrich, K. P. de Jong and P. E. de Jongh, *Nat. Mater.*, 2013, **12**, 34.

28 K. Spyrou, D. Gournis and P. Rudolf, *ECS J. Solid State Sci. Technol.*, 2013, **2**, 3160.

29 V. Tozzini and V. Pellegrini, *Phys. Chem. Chem. Phys.*, 2013, **15**, 80.

30 A. A. Balandin, S. Ghosh, W. Bao, I. Calizo, D. Teweldebrhan, F. Miao and C. N. Lau, *Nano Lett.*, 2008, **8**, 902.

31 G. Liu, Y. Wang, C. Xu, F. Qiu, C. An, L. Li, L. Jiao and H. Yuan, *Nanoscale*, 2013, **5**, 1074.

32 E. S. Cho, A. M. Ruminski, Y. S. Liu, P. T. Shea, S. Kang, E. W. Zaia, J. Y. Park, Y. D. Chuang, J. M. Yuk and X. Zhou, *Adv. Funct. Mater.*, 2017, **27**, 1704316.

33 E. S. Cho, A. M. Ruminski, S. Aloni, Y. S. Liu, J. Guo and J. J. Urban, *Nat. Commun.*, 2016, **7**, 1.

34 S. Inagaki, S. Guan, T. Ohsuna and O. Terasaki, *Nature*, 2002, **416**, 304.

35 N. Mizoshita and S. Inagaki, *Angew. Chem., Int. Ed.*, 2015, **54**, 11999.

36 N. Mizoshita, T. Tani and S. Inagaki, *Chem. Soc. Rev.*, 2011, **40**, 789.

37 M. Kubo, K. Ishiyama, A. Shimojima and T. Okubo, *Microporous Mesoporous Mater.*, 2012, **147**, 194.

38 M. Kuroki, T. Asefa, W. Whitnal, M. Kruk, C. Yoshina-Ishii, M. Jaroniec and G. A. Ozin, *J. Am. Chem. Soc.*, 2002, **124**, 13886.

39 G. Kalantzopoulos, A. Enotiadis, E. Maccallini, M. Antoniou, K. Dimos, A. Policicchio, E. Klontzas, E. Tylianakis, V. Binas and P. Trikalitis, *Int. J. Hydrogen Energy*, 2014, **39**, 2104.

40 E. Thomou, E. K. Diamanti, A. Enotiadis, K. Spyrou, E. Mitsari, L. G. Boutsika, A. Sapalidis, E. M. Alfonsín,

O. De Luca and D. Gournis, *Front. Chem.*, 2020, **8**, 840.

41 Y. Oumellal, C. Zlotea, S. Bastide, C. Cachet-Vivier, E. Léonel, S. Sengmany, E. Leroy, L. Aymard, J. P. Bonnet and M. Latroche, *Nanoscale*, 2014, **6**, 14459.

42 Y. Liu, M. Heere, L. C. Vasquez, C. Paterakis, M. H. Sørby, B. C. Hauback and D. Book, *Int. J. Hydrogen Energy*, 2018, **43**, 16782.

43 A. V. Neimark, Y. Lin, P. I. Ravikovitch and M. Thommes, *Carbon*, 2009, **47**, 1617.

44 O. Ivashenko, H. Logtenberg, J. Areephong, A. C. Coleman, P. V. Wesenhagen, E. M. Geertsema, N. Heureux, B. L. Feringa, P. Rudolf and W. R. Browne, *J. Phys. Chem. C*, 2011, **115**, 22965.

45 J. F. Moulder, *Handbook of X-ray photoelectron spectroscopy*, Perkin-Elmer Corporation, Physical Electronics Division, Eden Prairie, Min., U.S.A., 1995.

46 G. Zhu, Y. Wang, X. Wang, F. Yu and J. D. Miller, *Colloids Surf., A*, 2018, **558**, 313.

47 F. Yan, K. Spyrou, E. Thomou, S. Kumar, H. Cao, M. C. Stuart, Y. Pei, D. Gournis and P. Rudolf, *Environ. Sci. Nano*, 2020, **7**, 424.

48 P. Liu, I. L. Moudrakovski, J. Liu and A. Sayari, *Chem. Mater.*, 1997, **9**, 2513.

49 I. Dékány, R. Krüger-Grasser and A. Weiss, *Colloid Polym. Sci.*, 1998, **276**, 570.

50 J. Rouquerol, F. Rouquerol, P. Llewellyn, G. Maurin and K. S. Sing, *Adsorption by powders and porous solids: principles, methodology and applications*, Academic Press, Cambridge, Mass., U.S.A., 2013.

51 U. Holzwarth and N. Gibson, *Nat. Nanotechnol.*, 2011, **6**, 534.

52 Q. Yang, J. Sha, L. Wang, J. Wang and D. Yang, *Mater. Sci. Eng., C*, 2006, **26**, 1097.

53 S. de Graaf, J. Momand, C. Mitterbauer, S. Lazar and B. J. Kooi, *Sci. Adv.*, 2020, **6**, 4312.

54 T. K. Nielsen, P. Javadian, M. Polanski, F. Besenbacher, J. Bystrzycki and T. R. Jensen, *J. Phys. Chem. C*, 2012, **116**, 21046.

55 Y. Jia, C. Sun, L. Cheng, M. A. Wahab, J. Cui, J. Zou, M. Zhu and X. Yao, *Phys. Chem. Chem. Phys.*, 2013, **15**, 5814.

56 C. M. Ghimbeu, K. Guérin, M. Dubois, S. Hajjar-Garreau and C. Vix-Guterl, *Carbon*, 2015, **84**, 567–583.

57 M. Konarova, A. Tanksale, J. N. Beltramini and G. Q. Lu, *Nano Energy*, 2013, **2**, 98.

58 Y. Wang, X. Chen, H. Zhang, G. Xia, D. Sun and X. Yu, *Adv. Mater.*, 2020, **32**, 2002647.

59 G. Mulas, R. Campesi, S. Garroni, E. Napolitano, C. Milanese, F. Dolci, E. Pellicer, M. D. Baró and A. Marini, *J. Alloys Compd.*, 2012, **536**, 236.

60 S. Zheng, F. Fang, G. Zhou, G. Chen, L. Ouyang, M. Zhu and D. Sun, *Chem. Mater.*, 2008, **20**, 3954.

61 P. Ngene, P. Adelhelm, A. M. Beale, K. P. de Jong and P. E. de Jongh, *J. Phys. Chem. C*, 2010, **114**, 6163.

62 A. Schneemann, J. L. White, S. Kang, S. Jeong, L. F. Wan, E. S. Cho, T. W. Heo, D. Prendergast and J. J. Urban, *Chem. Rev.*, 2018, **118**, 10775.

63 H. Wang, S. Zhang, J. Liu, L. Ouyang and M. Zhu, *Mater. Chem. Phys.*, 2012, **136**, 146.

64 R. Gosalawit-Utke, T. K. Nielsen, I. Saldan, D. Laipple, Y. Cerenius, T. R. Jensen, T. Klassen and M. Dornheim, *J. Phys. Chem. C*, 2011, **115**, 10903.

65 A. Kaur, P. Chahal and T. Hogan, *EEE Electron Device Lett.*, 2015, **37**, 142–145.

66 X. Lu, Y. Zuo, X. Zhao and Y. Tang, *Corros. Sci.*, 2012, **60**, 165.

67 M. Santamaria, F. Di Quarto, S. Zanna and P. Marcus, *Electrochim. Acta*, 2007, **53**, 1314.

68 O. Friedrichs, J. Sánchez-López, C. López-Cartes, M. Dornheim, T. Klassen, R. Bormann and A. Fernández, *Appl. Surf. Sci.*, 2006, **252**, 2334.

69 Y. Zhang, L. Zhu, L. Chen, L. Liu and G. Ye, *Rev. Adv. Mater. Sci.*, 2019, **58**, 32.

70 L. Yan, J. Zhuang, X. Sun, Z. Deng and Y. Li, *Mater. Chem. Phys.*, 2002, **76**, 119.

71 R. Larciprete, S. Fabris, T. Sun, P. Lacovig, A. Baraldi and S. Lizzit, *J. Am. Chem. Soc.*, 2011, **133**, 17315.

72 S. C. Chang and M. H. Huang, *Inorg. Chem.*, 2008, **47**, 3135.